

New insights into time-series analysis IV: panchromatic and flux-independent period finding methods

C. E. Ferreira Lopes¹,¹★ N. J. G. Cross²★ and F. Jablonski¹

¹National Institute For Space Research (INPE/MCTI), Av. dos Astronautas, 1758 – São José dos Campos, SP-12227-010, Brazil

²SUPA (Scottish Universities Physics Alliance) Wide-Field Astronomy Unit, Institute for Astronomy, School of Physics and Astronomy, University of Edinburgh, Royal Observatory, Blackford Hill, Edinburgh EH9 3HJ, UK

Accepted 2020 December 21. Received 2020 December 18; in original form 2020 September 22

ABSTRACT

New time-series analysis tools are needed in disciplines as diverse as astronomy, economics, and meteorology. In particular, the increasing rate of data collection at multiple wavelengths requires new approaches able to handle these data. The panchromatic correlated indices $K_{(fi)}^{(s)}$ and $L_{(pfc)}^{(s)}$ are adapted to quantify the smoothness of a phased light-curve resulting in new period-finding methods applicable to single- and multiband data. Simulations and observational data are used to test our approach. The results were used to establish an analytical equation for the amplitude of the noise in the periodogram for different false alarm probability values, to determine the dependency on the signal-to-noise ratio, and to calculate the yield rate for the different methods. The proposed method has similar efficiency to that found for the string length period method. The effectiveness of the panchromatic and flux-independent period finding methods in single as well as multiple wavebands that share a fundamental frequency is also demonstrated in real and simulated data.

Key words: methods: analytical – methods: data analysis – methods: statistical – techniques: photometric – astronomical data bases: miscellaneous – surveys.

1 INTRODUCTION

If the brightness variations of a variable star are periodic, one can fold the sparsely sampled light curve with that period and inspect the magnitude as a function of phase plot. This will be equivalent to all the measurements of the star brightness taken within one period. The shape of the phased light curve and the period allow one to determine the physical nature of variability (pulsations, eclipses, stellar activity, etc.). If the light curve is folded with a wrong period, the magnitude measurements will be all over the place rather than align into a smoothly varying function of the phase. Other methods figure out the best period fitting a specific model into the phased light curve, like a sine function. The most common methods used in astronomy are the following: the Deeming method (Deeming 1975), phase dispersion minimization (PDM, Stellingwerf 1978; Dupuy & Hoffman 1985), string length minimization (SLM, Lafler & Kinman 1965; Dworetzky 1983; Stetson 1996; Clarke 2002), information entropy (Cincotta, Mendez & Nunez 1995), the analysis of variance (ANOVA, Schwarzenberg-Czerny 1996), and the Lomb–Scargle periodogram and its extension using error bars (LS and LSG, Lomb 1976; Scargle 1982; Zechmeister & Kürster 2009). All of these methods require as input the minimum frequency (f_{\min}), the maximum frequency (f_{\max}), and the sampling frequency (or the number of frequencies tested – N_{freq}). The input parameters and their constraints to determine reliable variability detections were addressed by Ferreira Lopes, Cross & Jablonski (2018), where a summary of recommendations on how to determine the sampling

frequency and the characteristic period and amplitude of the detected variations is provided. From these constraints, a good period finding method should find all periodic features if the time-series has enough measurements covering nearly all variability phases (Carmo et al. 2020).

Light-curve shape, non-Gaussianity of noise, non-uniformities in the data spacing, and multiple periodicities modify the significance of the periodogram and to increase completeness and reliability, more than one period finding method is usually applied to the data (e.g. Angeloni et al. 2012; Ferreira Lopes et al. 2015a, c). The capability to identify the ‘true’ period is increased by using several methods (see Section 4.3). However, this does not prevent the appearance of spurious results. Therefore, new insights into signal detection which provide more reliable results are welcome mainly when the methods provide dissimilar periods. Moreover, the challenge of big-data analysis would benefit a lot from a single and reliable detection and characterization method. This paper is part of a series of studies performed in the project called New Insight into Time Series Analysis (NITSA), where all steps to mining photometric data on variable stars are being reviewed. The selection criteria were reviewed and improved (Ferreira Lopes & Cross 2016, 2017), optimized parameters to search and analyse periodic signals were introduced (Ferreira Lopes et al. 2018), and now new frequency finding methods are proposed to increase our inventory of tools to create and optimize automatic procedures to analyse photometric surveys. The outcome of this project is crucial if we are to efficiently select the most complete and reliable sets of variable stars in surveys like the VISTA Variables in the Via Lactea (VVV, Minniti et al. 2010; Angeloni et al. 2014), Gaia (Gaia Collaboration et al. 2016), the Transiting Exoplanet Survey

* E-mail: ferreiralopes1011@gmail.com (CEFL); njc@roe.ac.uk (NJGC)

Satellite (Ricker et al. 2015), the Panoramic Survey Telescope and Rapid Response System (Pan-STARRS, Chambers et al. 2016), a high-cadence All-sky Survey System (Tonry et al. 2018), Zwicky Transient Facility (Bellm et al. 2019) as well as the next generation of surveys like PLANetary Transits and Oscillation of stars (Rauer et al. 2014), and Large Synoptic Survey Telescope (Ivezic et al. 2008).

Many efforts are being performed to generalize for multiband data the period finding methods. Süveges et al. (2012) utilized the principal component analysis to optimally extract the best period using multiband data. However, the multiband observations must be taken simultaneously that impose an important limitation to the method. On the other hand, VanderPlas & Ivezić (2015) introduce a general extension of the LS method, while Mondrik, Long & Marshall (2015) for the ANOVA from single-band algorithm to multiple bands not necessarily taken simultaneously. Indeed, methods combining the results from two different classes of period-determination algorithms are also being reached (Saha & Vivas 2017). The current paper adds one piece to this puzzle. Section 2.1 describes the new set of periodic signal detection methods as well as their limitations and constraints. Next, numerical simulations are used to test our approach in Section 3. From this, the efficiency rate and the fractional fluctuation of noise (FFN) are determined. Real data are also used to support our final results (see Section 4). Finally, our conclusions are presented in Section 5.

2 PANCHROMATIC AND FLUX-INDEPENDENT FREQUENCY FINDING METHODS

The Welch–Stetson variability index (Stetson 1996) was generalized and new ones were performed by Ferreira Lopes & Cross (2016). From where the panchromatic and flux-independent variability indices were proposed. These indices are used to discriminate variable stars from noise. To summarize, the panchromatic index is related to the correlation amplitude (or correlation height), while the second one computes the correlation sign, that is, if the correlation value is negative or positive without taking into account the amplitude. The flux-independent index provides correlation information that is weakly dependent on the amplitude or the presence of outliers. These features enable us to reduce the misclassification rate and improve the selection criteria. Moreover, this parameter is designed to compute correlation values among two or more observations. The correlation order (s), gives the number of observations correlated together, that is, $s = 2$ means correlation computed between pairs of observations and $s = 3$ means that correlations are computed on triplets. However, these observations must be close in time, that is, those observations are taken in an interval time smaller much less than the main variability period. Inaccurate or incorrect outputs will be obtained if this restriction is not enforced. Therefore, the data sets and sources with observations close in time were named as correlated data otherwise non-correlated data.

The efficiency rate to detect variable stars is maximized using the panchromatic and flux-independent variability indices when the number of correlations is increased, that is, when there is a strong variability between bins, but only slight differences between the measurements in each correlation bin. These variability indices only use those measurements that are close in time (i.e. a time interval much smaller than the variability period) and hence this constraint substantially reduced the number of possible correlations for sparse data. If we consider a light curve folded on its true variability period, with little noise, we could calculate these indices using standard correlated observations grouped in time, missing the observations

where too few meet the criteria of having at least s closer than ΔT in time. Alternatively, all measurements can be used to compute the indices if the observations are grouped by phase instead of time. It is the main idea to support the panchromatic and flux-independent frequency finding methods.

For the main variability period, the observations closed in phase should return strong correlation values. Since many variable stars show most variation as a function of phase, and little variation from period to period, recalculating the indices this way should return indices that are as strong as those grouped by time. On the other hand, if the light curve is folded on an incorrect period and the calculated phase is no longer a useful correlation measure, so correlations will be weaker, much like adding more noise to the data. The statistics considered in this paper are unlikely to be useful for data with multiple periodicities or if noise keeps its autocorrelation for phased data. In the next section, we propose an approach to compute the panchromatic and flux-independent indices in phase and hence provide a new period finding method.

Be aware that, the definition of expected noise performed by Ferreira Lopes et al. (2015a) needs to be corrected, as pointed by the referee of the current paper. The authors provided the correct theoretical definition of expected noise but the mathematical expression was incorrect. In the case of statistically independent events, the probability that a given event will occur is obtained by dividing the number of events of the given type by the total number of possible events, according to the authors. There will always be two desired permutations (either all positive or all negative) for any s value. However, the total number of events is 2^s , not s^2 as defined by the authors. The correct definition for expected noise value is then given by,

$$P_s = \frac{2}{2^s} = 2^{(1-s)} \quad (1)$$

The relative differences between the old and new definition for $s = 2$ and 4 are zero, while for $s = 3$ is ~ 11 per cent. However, for s values larger than 4 these differences increase considerably. The authors have only used the noise definitions to set the noise level for s values smaller than 4 , so far. Therefore, this mistake has not provided any significant error in the results of the authors to date.

2.1 New frequency finding methods

In common to other frequency finding methods, in our approach the light-curve data are folded with a number of trial frequencies (periods). The trial frequency that produces the smallest scatter in the phase diagram according to some criteria is taken as the estimate of the real period of variations. In our approach, we combine data from multiple bands with special transformations and characterize the phase diagram scatter using variability indices calculated from correlations of the phases (rather than correlations in the observation times, as they were used in previous works). The even statistic (for more details, see Paper II – Ferreira Lopes & Cross 2017) was used to calculate the mean, median, and deviation values. It only requires that the data must have even number of measurements (and if there is an odd number, the median value is not used), while the equations to compute these parameters are equal to the previous ones. This statement will be more important when the data have only a few measurements. On the other hand, these parameters assume equal values to the previous ones when the data have even number of measurements and they are quite similar for large data samples (typically bigger than 100).

Consider a generic time-series observed in multiple wavebands with observations not necessarily taken simultaneously in each band. This could also mean a time-series of the same sources taken by different instruments in single or multiwavelength observations. The subindex w is used to denote each waveband. Using this notation, all data are listed in a single table where the i th observation is $[t_{i,w}, \delta_{i,w}]$ where $\delta_{i,w}$ is given by

$$\delta_{i,w} = \sqrt{\frac{n_w}{n_w - 1}} \cdot \left(\frac{y_{i,w} - \bar{y}_w}{\sigma_{i,w}} \right), \quad (2)$$

where n_w is the number of measurements, $y_{i,w}$ are the flux measurements, \bar{y}_w is the even-mean computed using those observations inside of a 3σ clipped absolute even-median deviation (for more details, see Paper II – Ferreira Lopes & Cross 2017), and $\sigma_{i,w}$ denotes the flux errors of waveband w . One should note that greater success in searching for signals in multiband light curves is found when a penalty and an offset between the bands are used (for more details, see Long, Chi & Baraniuk 2014; VanderPlas & Ivezić 2015; Mondrik et al. 2015). However, these modifications require a more complex model since more constraints need to be added. For our purpose, we suppose that all wavebands used are well populated in order to provide a good estimation of the mean value.

The vector given by $[t_{i,w}, \delta_{i,w}]$ values contains data measured in either a single or multiwavebands. For instance, w assumes a single value if a single waveband is used. Therefore, the w subindex is only useful to discriminate different wavebands and to compute the $\delta_{i,w}$. To simplify, the w subindex is suppressed in the following steps. Therefore, the notation regarding all observations (N), observed in single or multiwavebands by a single or different telescopes, is given by $[(t_1, \delta_1), (t_2, \delta_2), \dots, (t_N, \delta_N)]$. From which, the panchromatic ($PL^{(s)}$) and flux-independent ($PK^{(s)}$) period finding indices are proposed as following;

(i) First, consider a frequency sampling $F = [f_1, f_2, \dots, f_{N_{\text{freq}}}]$.

(ii) Next, the phase values $\Phi' = [\phi'_1, \phi'_2, \dots, \phi'_N]$ are computed by $\phi'_i = t_i \times f_1 - \lfloor t_i \times f_1 \rfloor$, where t_i is the time and the $\lfloor \rfloor$ means the ceiling function of $t_i \times f_1$.

(iii) The phase values are re-ordered in ascending sequence of phase where $\Phi = [\phi_1, \phi_2, \dots, \phi_N]$ and $\phi_i \leq \phi_j$ for all $i < j$, and the δ_i are also re-ordered with their respective phases. Where for each phase value we have $[(\phi_1, \delta_1), (\phi_2, \delta_2), \dots, (\phi_N, \delta_N)]$.

(iv) Next, the following parameter Q of order s is computed as;

$$Q_i^{(s)} = \Lambda_{i, \dots, i+s-1}^{(s)} \sqrt{|\delta_i \dots \delta_{i+s-1}|} \quad (3)$$

where the $\Lambda^{(s)}$ function is given by

$$\Lambda_i^{(s)} = \begin{cases} +1 & \text{if } \delta_i > 0, \dots, \delta_{i+s-1} > 0; \\ +1 & \text{if } \delta_i < 0, \dots, \delta_{i+s-1} < 0; \\ 0 & \text{if } \delta_i = 0, \dots, \delta_{i+s-1} = 0; \\ -1 & \text{otherwise.} \end{cases} \quad (4)$$

Since we are assuming that the variables are periodic, when the period is correct, $\phi \sim 0$ should be equivalent to $\phi \sim 1$, so the last phases can be correlated with the first phases, that is, if $s = 2$, $Q_N^{(s)}$ correlates δ_N with δ_1 , and if $s = 3$, $Q_{N-1}^{(s)}$ correlates δ_{N-1} with δ_N and δ_1 , and $Q_N^{(s)}$ correlates δ_N with δ_1 and δ_2 , and so on. This consideration ensures the non-repetition of any term and keeps the number of $Q^{(s)}$ terms equal to the number of observations. The subindex s sets the number of observations that will be combined (for more details, see Paper I – Ferreira Lopes & Cross 2016).

(v) Finally, the period indices, equivalent to the flux-independent and panchromatic indices are given by,

$$PK^{(s)} = \frac{N^{(+)}}{N} \quad (5)$$

and,

$$PL^{(s)} = \frac{1}{N} \sum_{i=1}^N Q_i^{(s)}, \quad (6)$$

where $N^{(+)}$ means the total number of positive correlations (see equation 4). Indeed, the total number of negative correlations ($N^{(-)}$) is given by $N^{(-)} = N - N^{(+)}$.

(vi) The steps (ii)–(v) are repeated for all frequencies, f_1 to $f_{N_{\text{freq}}}$.

One should be aware that $\delta_{i,w}$ values are strongly dependent on the average and hence incorrect values can be found for Algol - type variable stars and time-series which have outliers, for example. In order to more accurately measure the average value only those observations within three times the absolute even-median deviations of the even median were used to do this. Additionally, $\Lambda^{(s)}$ is a bit different from that proposed for the flux-independent variability indices. The current version assumes $\Lambda^{(s)} = 0$ if $\delta_i = 0 \dots \delta_{i+s-1} = 0$. This would produce $PK^{(s)}$ and $PL^{(s)}$ equal zero in the trivial case of all observations being exactly equal, for example, a noiseless non-variable example, that is, $y_i = y_j$ for all i values (see two last panels of Fig. 2).

2.2 The maximum $PK^{(s)}$ considering different signals

The maximum value allowed for the $PK^{(s)}$ parameter considering the true variability frequency (f_{true}) of a signal is limited by the number of measurements which lead to $\Lambda^{(s)} = -1$, that is, the minimum number of times that one of the consecutive phase observations has a value on the opposite side of the even mean ($N_{(c)}$). This restriction limits the maximum value achievable by $PK^{(s)}$ ($PK_{(\text{max})}^{(s)}$). $PK_{(\text{max})}^{(s)}$ also varies with the order, s , since the number of $\Lambda^{(s)} = -1$ corresponding to observations on opposite sides of the even mean varies with s . Indeed, $N_{(c)}$ depends on the shape of the signal. For instance, $N_{(c)} = 1$ for a line, $N_{(c)} = 2$ for a sinusoidal signal, and $N_{(c)} = 4$ for a eclipsing binary light curve. Moreover, if a set of measurements is given by a line $y = ax + b$ ($a \neq 0$), the number of negative correlation measurements will be $N_{(\text{min})}^- = 1$ for $s = 2$, $N_{(\text{min})}^- = 2$ for $s = 3$, and $N_{(\text{min})}^- = 3$ for $s = 4$. Therefore, $N_{(\text{min})}^-$, and hence the maximum $PK^{(s)}$ value, varies with s . These considerations can be expressed as following $N_{(\text{min})}^- = N_{(c)} \times (s - 1)$. Lastly, the general relation for $PK_{(\text{max})}^{(s)}$ can be written as

$$PK_{(\text{max})}^{(s)} = 1 - \frac{N_{(\text{min})}^-}{N} = 1 - \frac{N_{(c)} \times (s - 1)}{N}. \quad (7)$$

A similar analytic equation for $PL^{(s)}$ index is not possible since it depends on the amplitude. On the other hand, two features of $PK^{(s)}$ can be seen in equation (7). First, $PK_{(\text{max})}^{(s)}$ values computed for two time-series having the same $N_{(\text{min})}^-$ value but a different number of observations differ (see Fig. 1). Second, all frequencies close to f_{true} produce $PK^{(s)} \simeq PK_{(\text{max})}^{(s)}$, since $N \gg N_{(\text{min})}^-$. These frequencies include the sub-harmonic frequencies of f_{true} . Indeed, f_{true} will always return the $PK_{(\text{max})}^{(s)}$ value for time-series models or signals without noise (see blue lines on Fig. 2). However, when noise is included, statistical fluctuations can lead to the wrong identification of f_{true} . This means that the $PK^{(s)}$ and consequently $PL^{(s)}$ parameters can return a main frequency that implies a smooth phase diagram but is different to f_{true} .

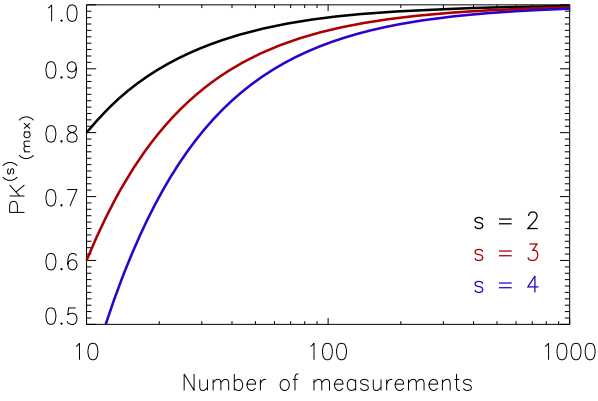


Figure 1. The $PK_{(\max)}^{(s)}$ as function of number of measurements for a sinusoidal function (see equation 7) for $s = 2$ (solid black line), $s = 3$ (solid red line), and $s = 4$ (solid blue line) where $N_{(\min)}^- = 2$ was adopted.

The values of $N_{(c)}$ and therefore $N_{(\min)}^-$ depend on the arrangement of observations around the even mean and are intrinsically related to the signal-to-noise ratio (S/N) as discussed above (see Fig. 2). For instance, the detached eclipsing binary (EA) signal looks like noise if only the measurements outside of the eclipse are observed, for example, if the phase fraction of the eclipses is $\lesssim \frac{2}{N}$. This means that the detection of the correct period using the $PK^{(s)}$ and $PL^{(s)}$ parameters will be extremely dependent on the number of observations at the eclipses. On the other hand, the RR Lyr (RR) objects show a small dispersion around the even mean even if the S/N is a bit low. To summarize, the $PK^{(s)}$ power will have a peak for all frequencies which produce smooth phase diagrams, with the largest spectrum peak corresponding to the smallest $N_{(\min)}^-$. On the other hand, the $PK_{(\max)}^{(s)}$ results in discrete values and so is more degenerate for a small number of observations.

Fig. 2 shows the phase diagrams for a Cepheid (Ceph), an RR Lyrae (RR), an RR Lyrae having the Blazhko effect (RRblz), eclipsing binaries (EA and EB), a rotational variable (Rot), and two white noise light curves generated by uniform and normal distributions (for more details see Section 3). One thousand equally spaced phased measurements were used to plot each model and to compute the $PK^{(s)}$ shown in each panel ($PK_{(\text{Model})}^{(s)}$). For these examples, we normalize amplitude to allow us to separate out the effects of the morphology of the light curves on these indices. As already mentioned, $PK^{(s)}$ is not directly dependent on the amplitude of the signal, as opposed to $PL^{(s)}$, which is. As expected, the model crosses the even-mean twice ($N_{(\min)}^- = 2$) for the Ceph, RR, RRblz, and Rot models giving $PK_{(\max)}^{(2)} = 0.998$. For the eclipsing binaries, the model crosses the even mean four times, implying a $PK_{(\max)}^{(2)} = 0.996$. Actually, the EA and EB models have $PK_{(\max)}^{(2)} = 0.994$ due to fluctuations of the model about the even median. Uniform and normal distributions (i.e. time-series mimicking noisy data) $PK_{(\max)}^{(2)} = \gamma + 2^{1-s}$ where γ is a positive number related with the maximum fluctuation of positive correlations. However, the $PK_{(\max)}^{(s)} = 1$ only happens when $\delta_i = 0 \forall i$ values, that is, noiseless non-variation.

The $PL^{(s)}$ values for the data are biased by the amplitude, that is, signals having different amplitudes will provide distinct values. Consider the index values computed using the data: the EA and EB signals have the smallest $PL^{(2)}$ values among all model tested due to their morphology, since the majority of measurements are near to the even mean and hence the peak power is reduced. The Ceph, RR, and RRblz signals usually have large amplitudes and hence

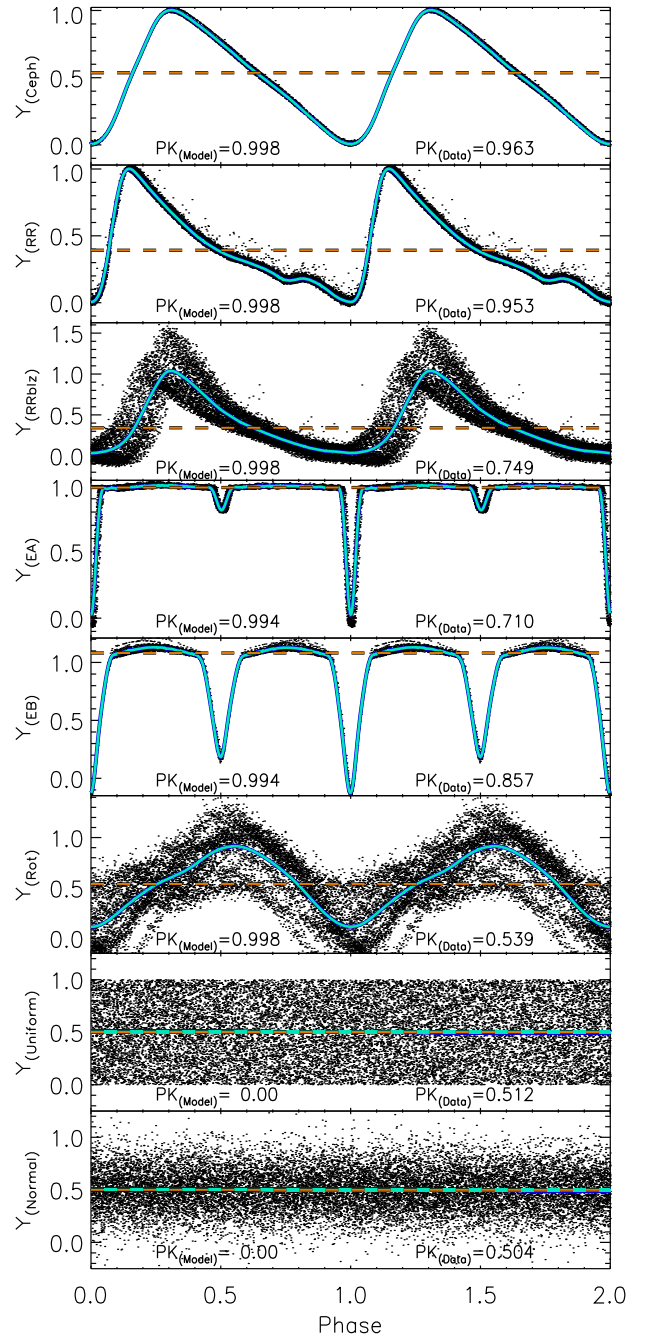


Figure 2. Phase diagrams for pulsating stars (RR, Ceph, and RRblz), eclipsing binaries (type EA and EB), rotational variable stars (Rot), and white noise from uniform and normal distributions. The data and model are shown as black dots and solid lines, respectively. The even-mean value considering those measurements within three times the absolute even-median deviation is shown as orange dashed lines. Moreover, the $PK^{(2)}$ and $PL^{(2)}$ values for the real and modelled data are displayed at the bottom of each diagram.

large $PL^{(2)}$ values. The highest $PL^{(2)}$ values are found for RR and Ceph signatures since there are a larger fraction of measurements distant from the even-mean than for the other models. The $PL^{(2)}$ value for RR stars is about half that found for the Rot model. This is a property related to the morphology of the phase diagram. Finally, the smallest values are found for pure-noise signals (normal and uniform distributions).

An examination of equation (7) can be used to estimate the theoretical expected value for any signal type. However, in real data, where noise is included, the $PK_{(\max)}^{(s)}$ values are smaller (see Fig. 2) since the values decrease with the increase in the dispersion of individual measurements about the even- \backslash mean. Therefore, *Rot* and *EA* models have the largest reduction in $PK_{(\max)}^{(s)}$. In contrast, the smallest reduction of $PK_{(\max)}^{(s)}$ is found for *Ceph* and *RR* models since the dispersion about even mean is small. A detailed analysis of the weight of S/N on $PK^{(s)}$ for different signal types is performed in the Section 3.

2.3 The optimal s value

The optimal s value ($s_{(\text{opt})}$) will be found when the difference between $PK^{(s)}$ computed on the phase diagram folded using f_{true} ($PK_{(\max)}^{(s)}$) and those ones found at other frequencies $PK_{(\text{fother})}^{(s)}$ is maximum. This difference can be written as,

$$PK_{(\text{true})}^{(s)} - PK_{(\text{fother})}^{(s)} \simeq PK_{(\max)}^{(s)} - PK_{(\text{noise})}^{(s)} \quad (8)$$

where we consider that $PK_{(\text{fother})}^{(s)} \simeq PK_{(\text{noise})}^{(s)}$ and compare the expressions (7) and (8)

$$\frac{N_{\text{true}}^+}{N} \simeq 1 - \frac{N_{(c)} \times (s_{(\text{opt})} - 1)}{N} \quad (9)$$

and hence,

$$s_{(\text{opt})} \simeq 1 + \frac{(N - N_{\text{true}}^+)}{N_{(c)}}, \quad (10)$$

where N_{true}^+ is the number of positive correlations for $f = f_{\text{true}}$. Equation (10) provides the s value where the maximum difference between the $PK_{(\text{true})}^{(s)}$ and $PK_{(\text{fother})}^{(s)}$ is found.

For high-S/N light curves, that is, $N - N_{\text{true}}^+ \rightarrow N_{(c)}$, $s_{(\text{opt})} = 2$ since for this case $N_{\text{true}}^+ \rightarrow N$. Indeed, the N_{true}^+ is directly proportional to the S/N, while $N_{(c)}$ is the opposite, that is, the increase of S/N increases N_{true}^+ and decreases $N_{(c)}$. Therefore, for low-S/N $N_{\text{true}}^+ \rightarrow N/2$ and hence $s_{(\text{opt})} \approx 1 + N/2 \times N_{(c)}$. However, at the limit, $N_{(c)}$ also tends to $N/2$ and hence $s_{(\text{opt})} \approx 2$. To summarize, the choice of s value depends on the signal type and S/N, since $N_{(c)}$ and N_{true}^+ vary with both parameters. For instance, a large value of $N_{(c)}$ is expected for *EA* binary systems whatever its S/N and hence a small s value is recommended to increase the range of signal type detected. The choice of s value must take all of these properties into account.

3 NUMERICAL TESTS AND SIMULATIONS

Artificial variable stars were simulated using a similar set of models as those produced in Paper III (for more details, see Ferreira Lopes et al. 2018). Seven simulated time-series were created that mimic rotational variables ($Y_{(\text{Rot})}$), detached eclipsing binaries ($Y_{(\text{EA})}$), eclipsing binaries ($Y_{(\text{EB})}$), pulsating stars ($Y_{(\text{Ceph})}$, $Y_{(\text{RR})}$, $Y_{(\text{RRblz})}$), and white noise ($Y_{(\text{Uniform})}$ and $Y_{(\text{Normal})}$). The *Ceph*, *RR*, *RRblz*, *EA*, and *Rot* models were based on the *CoRoT* light curves *CoRoT-211626074*, *CoRoT-101370131*, *CoRoT-100689962*, *CoRoT-102738809*, and *CoRoT-110843734*, respectively. The variability types were previously identified by Debosscher et al. (2007), Poretti et al. (2015), Paparó et al. (2009), Chadid et al. (2010), Maciel, Osorio & De Medeiros (2011), Carone et al. (2012), and De Medeiros et al. (2013), while the variability period and amplitudes were reviewed by Ferreira Lopes et al. (2018). The models of variable stars were found using harmonic fits having 12, 12, 12, 24, 24, and 6 coefficients for *Ceph*, *RR*, *RRblz*, *EA*, *EB*, and *Rot* variable

stars, respectively. The white noise simulations given by a normal distribution were used to determine the FFN. The *Ceph*, *RR*, *RRblz*, *EA*, and *Rot* models were used to realistically test and illustrate our approach.

The efficiency rate of any frequency finding method depends mainly on the signal type, the S/N ratio, and the number of observations. Therefore, three sets of simulations having 20, 60, and 100 measurements for an interval of S/N (see equation 11) ranging from ~ 1 to ~ 20 were created for the models found in Fig. 2. In particular, 20 per cent of measurements were randomly selected at the eclipses for *EA* and *EB* simulations. This is required because these simulations look like noise if no measurement is found at the eclipses, and is justified because any light curves that are processed with period-finding algorithms in NITSA must already have been selected as variables, so eclipsing binaries with few measurements must have a relatively high fraction at the eclipses. There will be a selection effect against binaries with narrow eclipses, since the probability of them being detected as variables is reduced. Values sorted randomly from a normal distribution were used to add noise to the simulations and the error bars were set to be the differences between the model and simulated data. The error bars are not relevant to compute the $PK^{(s)}$ values. However, they are necessary to determine $PL^{(s)}$ parameters. The S/N was computed as,

$$S/N = \frac{A}{2.96 \times eMAD(\delta_y)} \quad (11)$$

where A is the signal amplitude, δ_y are the residuals (observed minus its predicted measurement), and $eMAD$ is the even median of the absolute deviations from the even-median. The $eMAD$ is a slight modification of median absolute deviation from median (MAD). The $2.96 \times eMAD(\delta_y)$ is equivalent to two times the standard deviation but it is a robust estimate of the standard deviation when outliers are considered (e.g. Hoaglin, Mosteller & Tukey 1983). For completeness, other estimates of the S/N where the model is not required were tested (e.g. Rimoldini 2013). According to our tests, the latter usually overestimates the S/N compared with those values computed by equation (11).

3.1 Fractional fluctuation of noise

The FFN for signal detection is related to the level for which the figure of merit of the methods (e.g. power, in the classical periodogram) is not expected to exceed more than a fraction of times due to stochastic variation (or noise) on the input light curve. Indeed, the FFN mimics a false alarm probability since it sets the power value above which a certain percentage of spurious signals are found. Indeed, there are many difficulties of estimating FAPs in realistic astronomical time-series (for more detail, see Koen 1990; Sulis, Mary & Bigot 2017; VanderPlas 2018) and hence FFN only means the lower empirical limit to find a reliable signal. The expected value of the flux-independent index, $K_{\text{fl}}^{(s)}$, for white noise is analytical defined as $P_s = 2^s - 1$ (see Section 2). The same equation can be applied to $PK^{(s)}$ since $K_{\text{fl}}^{(s)}$ and $PK^{(s)}$ are based on the same concept. Therefore, the $FFN_{(s)}$ can be defined as,

$$FFN_{(s)} = P_s + \Delta = \sqrt{\frac{\alpha}{N}} + \beta \quad (12)$$

where α and β are real positive numbers. β must be larger than P_s since it is a threshold for white noise. 10^7 Monte Carlo simulations using a normal distribution were run with the number of measurements ranging from 10 to 1000 in order to compute the free parameters for equation (12). Fig. 3 shows the mean values of $PK^{(s)}$ above which

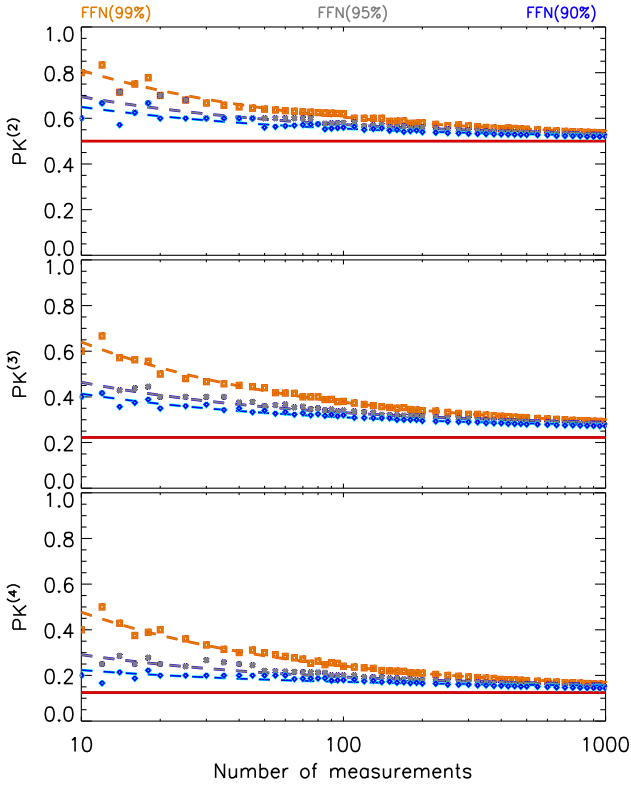


Figure 3. $PK^{(s)}$ as a function of the number of measurements for orders 2, 3, and 4. The results for significance levels of 99 per cent (orange), 95 per cent (grey), and 90 per cent (blue) are in different colours. The dashed lines indicate the $FFN_{(s)}$ for models while the solid, red line shows the expected value for the noise (see Section 3.1).

Table 1. The constraints to FFN_s models (see equation 12) which delimit 99 per cent, 95 per cent, and 90 per cent of white noise, respectively.

Order	99 per cent		95 per cent		90 per cent	
	α	β	α	β	α	β
$FFN_{(2)}$	0.9459	0.5107	0.5350	0.5177	0.4377	0.5112
$FFN_{(3)}$	1.2321	0.2541	0.6150	0.2696	0.4784	0.2625
$FFN_{(4)}$	1.0937	0.1316	0.4511	0.1482	0.2380	0.1482

1 per cent (orange dots), 5 per cent (grey dots), and 10 per cent (blue dots) of simulated data are found. The $FFN_{(s)}$ models are shown as dashed lines and the free parameters of the models are presented in Table 1. The minimum values of $FFN_{(s)}$ are found when $N \rightarrow \infty$. For this condition the $FFN_{(s)}$ estimates have values above the noise (see Table 1). The scatter found for small numbers of measurements (typically less than 20) is related to the discrete values allowed for $PK^{(s)}$ (for more details, see Ferreira Lopes & Cross 2016). The results shown in Fig. 3 are quite similar for all uncorrelated zero-mean noise distributions.

The $FFN_{(s)}$ can be used as a reference to remove unreliable signals that lead to random phase variations in any survey, whatever the wavelength observed. This property is related to the weak dependence of $PK^{(s)}$ on amplitude, error bars, or outliers according to Ferreira Lopes & Cross (2017). Indeed, spurious periods that lead to smooth phase diagrams will break this constraint. On the other hand, the period that produces the main peak in the periodogram can be related with a phase diagram which has gaps for common methods like PDM and LSG. This happens because the function

used to measure the periodogram can interpret this arrangement of measurements as a smooth phase diagram. This result can lead to the highest periodogram peak when the signal is not well defined and/or when a small number of epochs are available. On the other hand, the periods that lead to folded phase diagrams with gaps may not have many correlated measurements and hence they will not lead to peaks in the $PK^{(s)}$ and $PL^{(s)}$ periodogram. Indeed, the main peak of the periodogram will be the arrangement of measurements that leads to the largest correlation value.

3.2 Dependency on the signal-to-noise ratio

The *Ceph*, *RR*, *RRblz*, *EA*, *EB*, and *Rot* models (for more details, see Section 3) were used to analyse the $PK^{(s)}$ values for the main variability signal. $PK^{(s)}$ values were computed using 10^7 Monte Carlo simulations for S/N ranging from 1 to 20. The simulations were created for $s = 2, 3$, and 4. The results for $s = 3$ and 4 show lower efficiency than those found for $s = 2$ for lower S/N values, as expected from Section 2.3. The results for larger orders, s , provide better results than those found for $s = 2$, for high S/N time-series, having large number of measurements (see Section 2.3). Therefore, we only show the results for $s = 2$. Fig. 4 shows the $PK^{(s)}$ as function of S/N for $s = 2$. The results are displayed using box plots instead of error bars because $PK^{(s)}$ results in discrete values and its distribution is not symmetric. A box plot range that includes 90 per cent of results was used, and the red line sets the middle of the distribution. The main results can be summarized as follows:

(i) The maximum value achieved by $PK^{(s)}$ is limited by the number of measurements for all S/N . Moreover, this effect is also observed for higher s orders in agreement with the values estimated by equation (7) (see Fig. 1).

(ii) $PK^{(s)}$ tends to $PK^{(s)}_{(max)}$ for simulations using 20, 60, and 100 measurements and high S/N for *Ceph*, *RR*, *RRblz*, *EB*, and *Rot* models. The same trend having a slower growth is also observed for *EA*. Indeed, $PK^{(s)}$ values are improved for *EA* models when the number of measurements, mainly at the eclipses, is increased. About ~ 50 per cent of $PK^{(s)}$ values for $S/N = 3$ are found below the expected noise value when the time-series has 20 measurements. This number is reduced to less than ~ 10 per cent when more than 60 measurements are available.

(iii) The dispersion of $PK^{(s)}$ values decreases with the number of measurements for all values of S/N . The effect is less noticeable for *EA* models. This happens because the simulated time-series looks like noise when most of the measurements are sorted outside of eclipses.

(iv) About ~ 95 per cent of $PK^{(2)}$ values are above P_2 values for the whole range of S/N for *Ceph*, *RR*, *RRblz*, *EB*, and *Rot* simulations using 60 and 100 measurements. This is also true for the simulations containing 20 measurements for $S/N > 2$. On the other hand, the *EA* model shows $PK^{(2)}$ values around the noise level for the whole range of S/N on the simulations containing 20 measurements. The reason for this behaviour is the same as explained in the last item.

(v) The time-series like *EA* and *EB* models have the lowest $PK^{(s)}$ values among all models analysed.

In summary, the probability of finding $PK^{(s)}$ values above the noise is dependent on the number of measurements, S/N , and signal type, as expected. For all simulations, when the number of measurements is increased, we can measure reliable periods at lower S/N . The simulations for higher s order are quite similar to those found for $s = 2$.

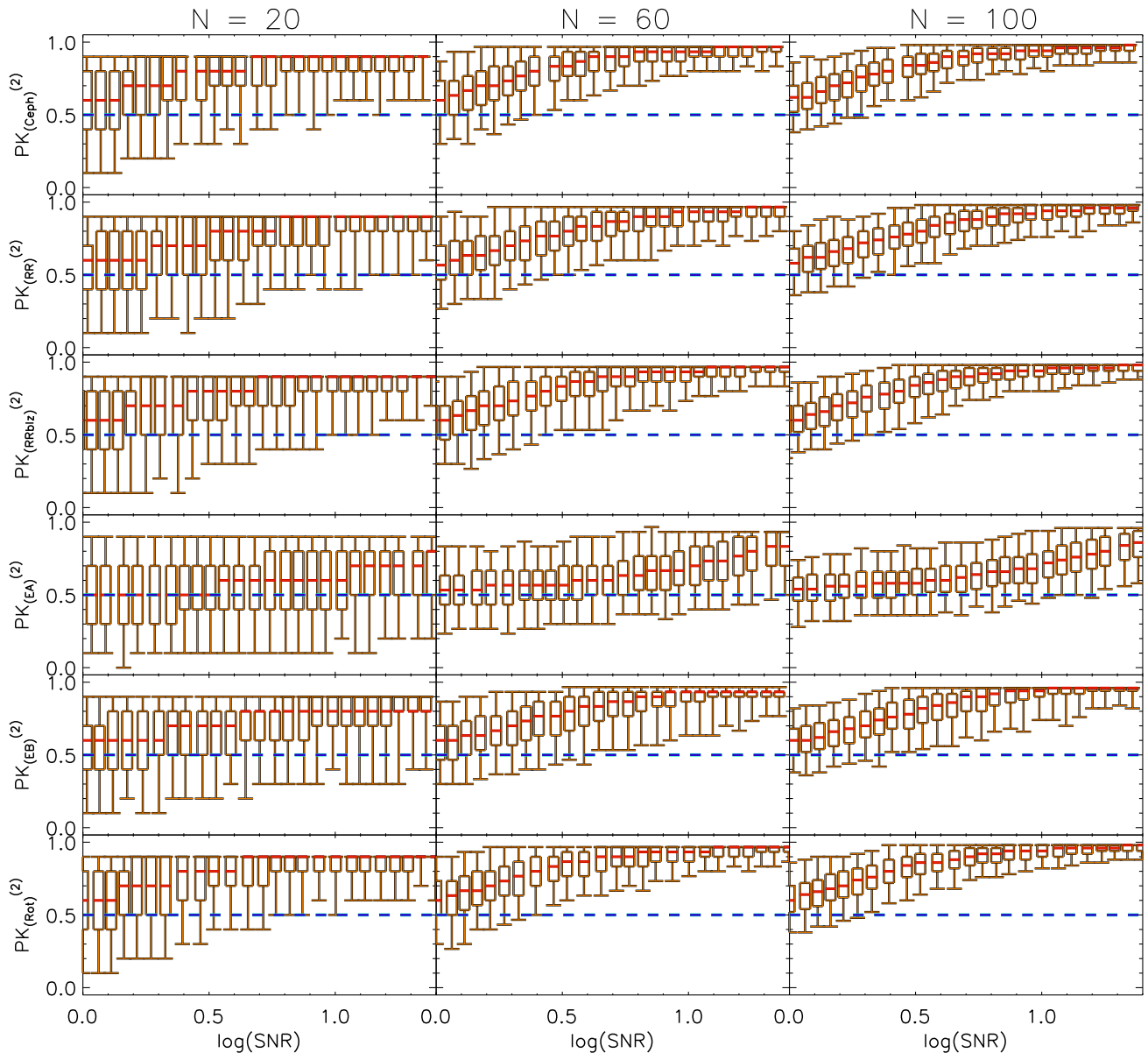


Figure 4. $PK^{(s)}$ as a function of S/N for order 2 ($s = 2$) for the variable stars models shown in the Fig. 2. Each column displays the results for 20 (left-hand column of panels), 60 (middle panels), and 100 (right-hand columns of panels) measurements while each row presents the results for different variable types: Cepheid, RRlyrae, RRblz, EA, EB, and Rot models. Box plots containing 90 per cent of the data are shown. The even-median values for each box are marked by a solid red line, while the dashed blue lines show the expected value for the noise.

4 TESTING THE METHOD ON REAL DATA

A robust numerical simulation is complex because it usually does not reproduce the correlated nature of the noise intrinsic to the data as well as variations related to the instrumentation. Many constraints are required to provide realistic simulations such as a wide range of amplitudes, error bars, outliers, and correlated noise, to name a few. However, the simulation of the $PK^{(s)}$ power is facilitated because: (i) the amplitude can be a free parameter since $PK^{(s)}$ is only weakly dependent on it; (ii) the even mean values (see equation 2) are computed using those observations within three times the absolute even-median deviation, which effectively reduces the outliers weight on zero-point estimation (\bar{y}_w , see equation 2) but all epochs are considered to compute the powers; and (iii) the correlated nature of successive measurements is reduced since they are computed using

phase diagrams. On the other hand, a robust simulation for $PL^{(s)}$ covering all important aspects of it is difficult because $PL^{(s)}$ has a strong dependence on amplitude, outliers, and error bars. Therefore, the discussions in the previous sections only address the constraints on $PK^{(s)}$.

The $PK^{(s)}$ and $PL^{(s)}$ methods can be tested on real data using existing variable stars catalogues. The WFCAMCAL variable stars catalogue (WVSCI) having 280 stars (Ferreira Lopes et al. 2015a) and the Catalina Survey Periodic Variable star catalogue (CVSCI) having ~ 47000 sources (Drake et al. 2014) were used to estimate the efficiency rate of our new period finding methods. The WVSCI was created from the analysis of the WFCAM Calibration 08B release (WFCAMCAL08B, Hodgkin et al. 2009; Cross et al. 2009). More information about the design, the data reduction, the layout, and

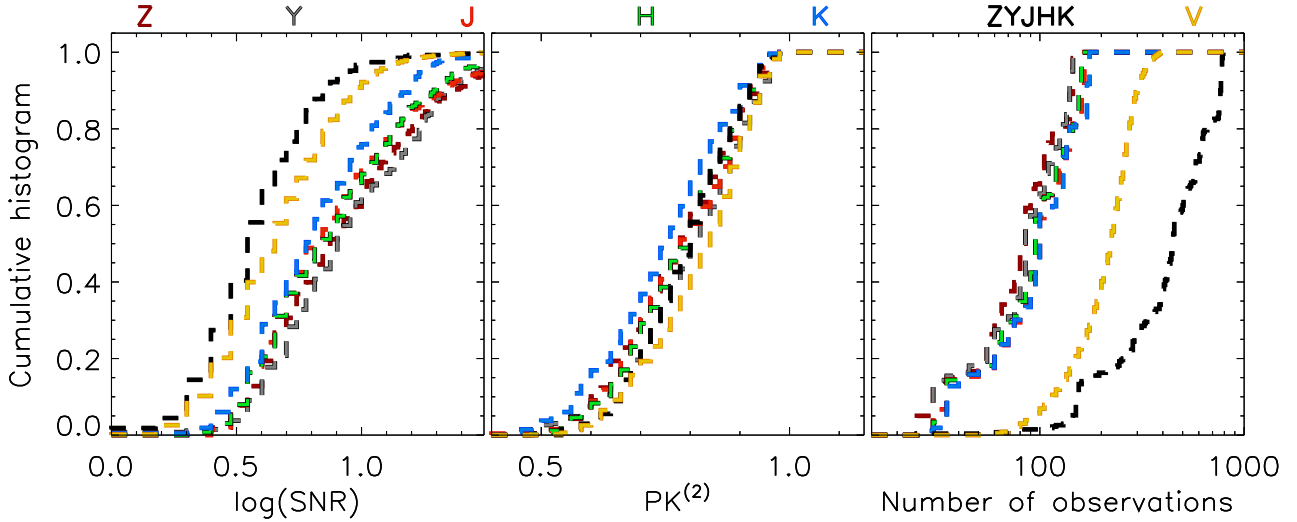


Figure 5. Cumulative histograms of S/N , PK^2 , and number of measurements for *WVSCI* and *CVSCI* stars. The results are shown for Z (brown), Y (grey), J (red), H (green), K (blue), V (yellow), as well as the panchromatic (black) data.

about variability analysis of this data base are described in detail in Hambly et al. (2008), Cross et al. (2009), and Ferreira Lopes et al. (2015a). The WFCAMCAL data base is a useful data set to test single and panchromatic wavelength period finding methods. To summarize, WFCAM data base contains panchromatic data (ZYJHK wavebands) that were observed to calibrate the UKIDSS surveys (Lawrence et al. 2007). A sequence of filters JHK or ZYJHK were observed within a few minutes during each visit the fields. These sequences were repeated in a semiregular way that leads to an uneven sampling having large seasonal gaps. On the other hand, the *CVSCI* has a huge amount of objects, with seventeen variable stars types that were visually inspected by the authors.

In order to perform a straightforward comparison between the results, the S/N of *WVSCI* and *CVSCI* stars were also estimated using equation (11). Also, the number of measurements and the $PK^{(2)}$ values were computed. Fig. 5 shows the cumulative histograms of S/N and number of measurements for *WVSCI* and *CVSCI* stars. The results for each waveband as well as for panchromatic data are shown by different colours. About ~ 90 per cent of *WVSCI* single waveband has $S/N > \sim 3$ while this number decreases to ~ 70 per cent for the *CVSCI* and panchromatic data. The *WVSCI* single waveband data have a number of measurements ranging from ~ 30 to ~ 150 , while *CVSCI* stars have a number from ~ 100 to ~ 300 . When the panchromatic data are considered, the number of measurements increases considerably by a factor ~ 5 compared with *WVSCI* single waveband. However, the S/N are smaller than those found for single wavebands. In general, the S/N for panchromatic wavebands are smaller than those found for *CVSCI* stars.

Understanding the peculiarities of the sample tested is crucial when analysing the efficiency rate of our approach. Therefore, we summarize how the period searches were performed to find periods for *WVSCI* and *CVSCI* stars. Ferreira Lopes et al. (2015a) selected about 6651 targets to which four period finding methods were applied. Next, the 10 best ranked periods in each of the four methods were selected. For each period, a light-curve model was created using harmonics fits. Finally, the very best period was chosen as that with the smallest χ^2 with respect to all ranked periods; on the other hand, the period search for $\sim 154\,000$ *CVSCI* sources was made using the LS method. Next, the main periods were analysed using

the Adaptive Fourier Decomposition method (Torrealba et al. 2015) in order to determine the main variability period and reduce the number of sources to be visually inspected (112 000). Additionally, the periods of a large number of the sources were improved and corrected by the authors. Many of the variability periods of *WVSCI* and *CVSCI* were related to subharmonics of their true period and the final results were set after visual inspection.

The following sections discuss the *WVSCI* and *CVSCI* variable stars from the viewpoint of $PK^{(s)}$ and $PL^{(s)}$ parameters. The periodogram, the efficiency rate, and the peculiarities of our approach are analysed. For that, we perform the period search using the SLM, LSG, and PDM methods besides the panchromatic and flux-independent methods. A frequency range of $(2/T_{\max})d^{-1}$ to $30d^{-1}$ was explored and we evenly sampled this frequency range with a frequency step of $\frac{1}{300 \times T_{\max}}$, where T_{\max} is the total time span. The frequency sampling constrains a maximum phase shift of 0.1 that allows us to detect the large majority of signal types (for more detail see Paper III). A quick visual inspection was performed on some of *WVSCI* and *CVSCI* to test our analysis in the next sections. The main goal of this work is to propose a new period finding method instead of checking the reliability of the periods in the *WVSCI* and *CVSCI* catalogues.

4.1 Periodogram and efficiency rate

The $PK^{(2)}$ and $PL^{(2)}$ periodograms were computed for the *WVSCI* and *CVSCI* stars. For better visualization, the differential panchromatic light curve (see Fig. 6) was obtained by subtracting the even median from the magnitudes in each light curve. As a result, light curves with zero mean are produced. The $PK^{(s)}$ and $PL^{(s)}$ parameters do not use any kind of transformation to combine measurements at different wavelengths. However, a better way to combine multiwavelength data is an open question.

Fig. 6 shows the phase diagrams and their normalized periodogram for some *WVSCI* stars. The phase diagrams (left-hand panels) show the folded panchromatic data, while the periodogram considering single and panchromatic wavebands are displayed in the centre and right-hand panels respectively. The periodogram for a large part of *CVSCI* stars are quite similar to those found for panchromatic data, that is, periodogram for sources having more measurements and

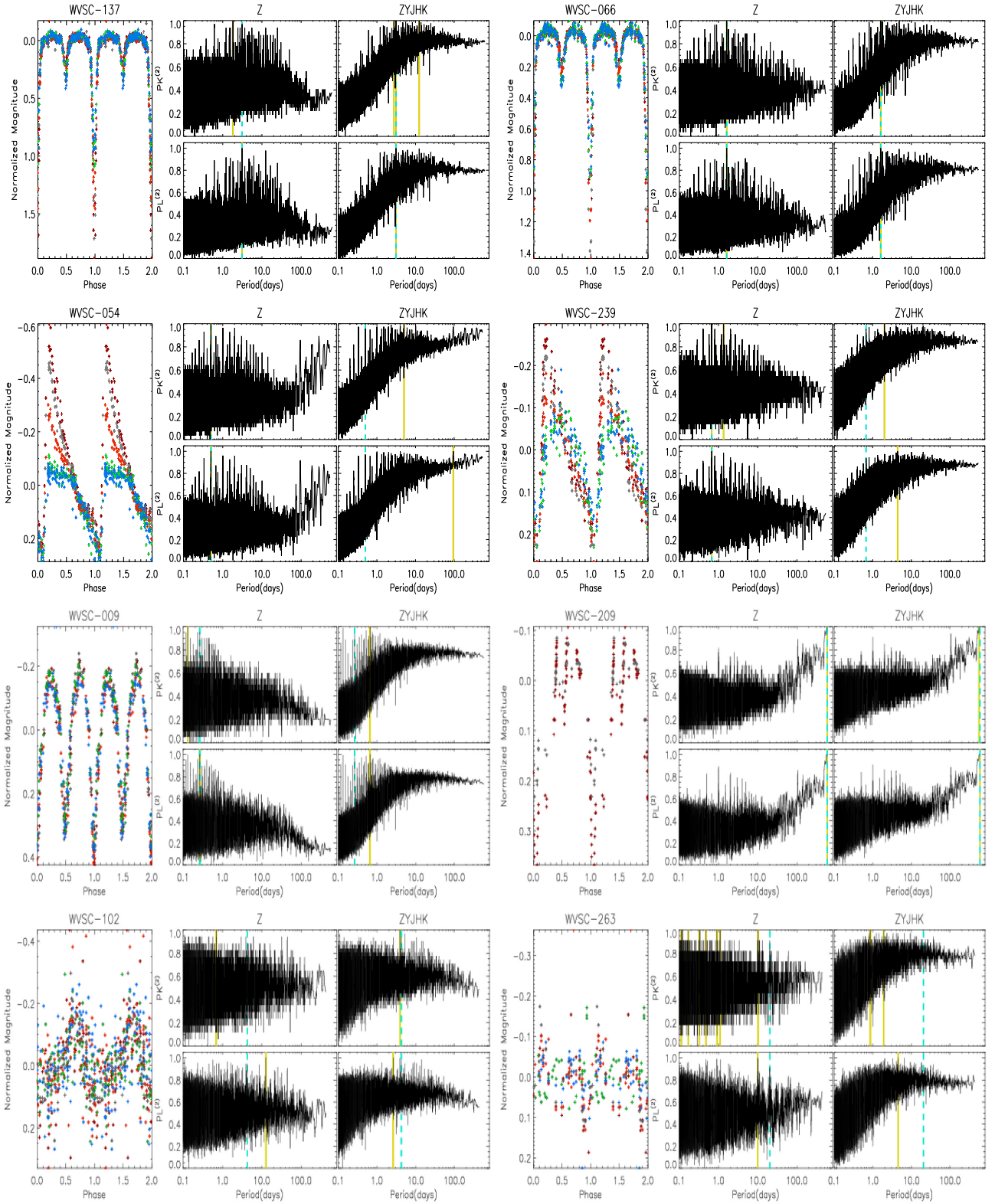


Figure 6. Phase diagrams of panchromatic data (left-hand panels) and the $PK^{(s)}$ and $PL^{(s)}$ normalized periodograms for Z and ZYJHK wavebands (right-hand panels). The cross symbols in the phase diagrams set the measurement of Z (brown), Y (grey), J (green), H (red), and K (blue) wavebands. The dashed green lines indicate the published variability periods, while the full yellow lines indicate the periods related with the largest peak in the periodogram.

smaller S/N than for the *WVSCI* single waveband. The main results can be summarized as follows:

(i) $PK^{(2)}$ has more than one peak related with the maximum power for *WVSC-239* and *WVSC-263*, that is, this means that $PK^{(s)}$ indicates more than one viable period. The number of such periods gives the ‘degeneracy’ of a particular arrangement of measurements in the phase diagram. This number increases as the number of measurements decreases (see equation 7).

(ii) The main period found by $PK^{(2)}$ is not the same as that obtained by $PL^{(2)}$. This means that the maximum number of positive correlations is not the same as the maximum correlation power. Besides, the ‘degeneracy’ of periods found for $PK^{(2)}$ is not observed in the $PL^{(2)}$ periodogram.

(iii) $PK^{(2)}$ and $PL^{(2)}$ periodograms for the *Z* waveband show a scatter around the expected noise level. Additionally, the *WVSC-054* and *WVSC-209* periodograms show an increase in $PK^{(2)}$ for long periods. Indeed, this behaviour is observed in all wavebands and hence it is an attribute of the proposed method.

(iv) $PK^{(2)}$ for panchromatic data increases with periods up to a maximum of around 5 d and then levels off and drops slightly for longer periods for almost all sources. These sources have variability periods of less than 5 d. This behaviour is not found for *WVSC-209* and *WVSC-102*. Indeed, *WVSC-102* has a variability period of 589 d and hence the trend observed is different to the others. On the other hand, *WVSC-209* has a low-S/N signal. Therefore, this trend is related with the variability period and S/N. Indeed, the phase diagram keeps part of the correlation information when the light curve is folded using a test period bigger than the true variability period.

(v) $PK^{(2)}$ and $PL^{(2)}$ periodograms have peaks at the previous measured (true) variability periods of *WVSCI* stars. However, the period related with the largest peak is not always the true variability period.

(vi) The panchromatic data have lower S/N. Indeed, no clear signal can be observed in *WVSC-263*. This could mean that the signal shape is very different from one band to another, or a signal or seasonal variation is present in a single waveband, or the variability period is wrong, to name the most likely possibilities.

To summarize, the $PK^{(s)}$ and $PL^{(s)}$ periodograms indicate the arrangement of measurements in the phase diagram that maximize the correlation signal and power, respectively. Therefore, the $PK^{(s)}$ and $PL^{(s)}$ parameters can be used to identify the periods that lead to a smooth phase diagram from the viewpoint of correlation strength.

4.2 Accuracy

The accuracy was measured considering the main signal(s) detected by the $PK^{(2)}$ and $PL^{(2)}$ methods. Indeed, the largest power of $PK^{(s)}$ periodogram can be related to more than one period. Therefore, all periods related to the largest periodogram peak were considered to measure the accuracy, that is, the recovery fraction of variability periods. Two parameters to measure the accuracy were considered: $E_{(M)}$ – when the main period is detected; $E_{(MH)}$ – when the main variability period (P_{Lit}), measured in Ferreira Lopes et al. (2015a), or its subharmonic, or overtone is found. Indeed, the processing time of each method was not taken into account in this discussion. A new approach to reduce the running time necessary to perform period searches will be addressed in a forthcoming paper in this series. Those signals found within ± 1 per cent of the variability period were considered as detected. Table 2 shows the results for individual wavebands as well as for the panchromatic data. The main results can be summarized as:

(i) The accuracy is lower than 100 per cent for all methods and data tested. However, new estimates of Catalina variability periods have been produced recently (e.g. Papageorgiou et al. 2018) and the *CVSCI* combines the results found by PDM, LSG, and STR methods for all wavebands to determine the best variability period. Therefore, the accuracy for both data sets is larger than that displayed in Table 2 if these results are taken into consideration.

(ii) $PK^{(2)}$ has the highest efficiency rate considering only the main period ($E_{(M)}$) for the *Z*, *Y*, *J*, *H*, and *K* wavebands. The efficiency rate of $PK^{(2)}$ for the *V* waveband and panchromatic data is similar to that found for the SLM and $PL^{(2)}$ methods. $E_{(M)}$ decreases from *Z* to *K* wavebands because the first ones have larger S/N.

(iii) The $E_{(MH)}$ values for *Z*, *Y*, *J*, *H*, and *K* for $PK^{(2)}$ and SLM are quite similar and they have the highest accuracy for the *Z* and *Y* wavebands. On the other hand, PDM has the highest $E_{(MH)}$ values for *H*, *ZYJHK*, and *V* wavebands. Indeed, the $E_{(MH)}$ values for PDM and LSG are quite similar for the *V* waveband.

(iv) The $E_{(M)}$ for $PL^{(2)}$ is always smaller than that found for $PK^{(2)}$ except for *V* band where it is 4 per cent lower for $PK^{(2)}$.

(v) The highest $E_{(M)}$ is found for $PK^{(2)}$ method while the highest $E_{(MH)}$ is found for the PDM method. The accuracy found for LSG method is quite similar to that found for PDM method for *V* waveband, while in other wavebands, the PDM method has twice the accuracy. Indeed, this difference is reduced by a few per cent if a higher relative error is considered. Indeed, the P_{Lit} found by the *ZYJHK* wavebands are refined using the SLM method (for more details, see Ferreira Lopes et al. 2015a). On the other hand, the *V* waveband results were computed using LS and refined using reduced χ^2 (for more details, see Drake et al. 2014). Therefore, the accuracy can be biased by the approach used to improve the variability period estimation. Indeed, a deep discussion about how to determine accurately the variability period and its error is found in the third paper of this series (for more detail, see Ferreira Lopes et al. 2018).

(vi) The panchromatic data do not significantly increase the efficiency rate for any method. The panchromatic data provides a larger number of measurements but a smaller S/N compared with those found for single wavebands (see Fig. 5).

(vii) The efficiency rate of $PK^{(2)}$, $PL^{(2)}$, and SLM is strongly decreased for *V* and panchromatic data. This is related with the smaller S/N of these data. It indicates a strong dependence of the $PK^{(2)}$ and $PL^{(2)}$ methods on the S/N.

The periods detected by PDM are also detected by the LSG method. Moreover, almost all periods detected using the PK, PL, and STR methods are also found by the LSG method. The periods detected using LSG or PDM which are not found by other methods belong mainly to a few types: W UMa (~ 61 per cent), EA (~ 13 per cent), RR Lyr on first overtone (~ 10 per cent), and RR Lyr on several modes (~ 2 per cent), measured using the ratio of the number of missed sources to the total number of sources missed. Indeed, the largest miss rate is found for the multiperiodic RR Lyr-type when the relative number of sources are considered, that is, the fraction of missed sources divided by the number of sources detected for each variability type. As expected, the multiperiodic periods have the largest miss rate since the current approach is not designed to select these periods. From quick visual inspection on phased data of the periods found by methods other than PDM and LSG the following concerns have been raised: the period found is a higher harmonic or overtone of that found in the literature; the phase diagram is not always smooth; the period found sometimes produces a smooth phase diagram but the period found is different or has a

Table 2. Accuracy considering two approaches; the main period ($E_{(M)}$) and the main period plus its subharmonic and overtone. We consider that there is agreement if the relative difference is smaller than 1 per cent.

	Z		Y		J		H		K		ZYJHK		V	
	$E_{(M)}$	$E_{(MH)}$	$E_{(M)}$	$E_{(MH)}$	$E_{(M)}$	$E_{(MH)}$	$E_{(M)}$	$E_{(MH)}$	$E_{(M)}$	$E_{(MH)}$	$E_{(M)}$	$E_{(MH)}$	$E_{(M)}$	$E_{(MH)}$
PK ⁽²⁾	0.30	0.55	0.30	0.59	0.30	0.60	0.29	0.59	0.23	0.50	0.19	0.40	0.24	0.51
PL ⁽²⁾	0.20	0.46	0.22	0.49	0.22	0.50	0.28	0.57	0.17	0.44	0.14	0.27	0.25	0.53
LSG	0.10	0.27	0.09	0.29	0.09	0.34	0.09	0.26	0.11	0.31	0.09	0.32	0.20	0.87
PDM	0.17	0.50	0.26	0.59	0.25	0.62	0.27	0.62	0.22	0.57	0.26	0.69	0.22	0.88
SLM	0.30	0.55	0.30	0.59	0.29	0.63	0.28	0.59	0.22	0.50	0.15	0.32	0.25	0.49

relative difference larger than 1 per cent. This means that STR, PK, and PL methods are more likely to return spurious periods or higher harmonics of the main variability period since the majority of the sources missed belong to these groups.

On the other hand, about ~ 8 per cent of the Catalina periods do not correspond to our periods. We also made a quick visual inspection of the phased data using the periods found by Catalina and those found by us. As a result, we verify that the large majority (more than ~ 70 per cent) of phase diagrams of this subsample produce smoother phase diagrams using our periods than those found using Catalina periods (see the third row of panels of Fig. 7). Indeed, this assumes that the true or main variability period should be that one which produces the smoothest phase diagram.

In summary, the $PK^{(s)}$ and $PL^{(s)}$ methods can be used as a new tool to find periodic signals. In fact, they are more efficient than all methods tested if high S/N data are considered. As a rule, the new approach can be used in the same fashion as other period finding methods. One should be aware that, the lower efficiency rate for small S/N, probable bias for longer periods, and the multiple periods given by $PK^{(s)}$ must be taken into account.

4.3 Cautionary notes on period searching

The main variability period is assumed to be that one which provides the smoothest phase diagram. Indeed, the periodicity of many signals in oversampled data like *CoRoT* and *Kepler* light curves (e.g. Paz-Chinchón et al. 2015; Ferreira Lopes et al. 2015b) can be easily identified by looking directly at the light curve. This may not include low S/N multiperiodic signals. On the other hand, the signals in undersampled data can only be identified by eye using phase diagrams. In both cases, the phase diagram should be smooth at the main variability period. However, more than one period can lead to smooth phase diagrams. In fact, due to the nature of the analysis of big data sets it is highly likely that some observational biases exist or that pathological cases arise where the combination of random or correlated errors, nearby sources, mimic expected variations. Therefore, additional information must be put together to solve this puzzle. For instance, photometric colours, amplitudes, nearby saturated sources, crowded sky regions, distances, and other information are crucial to confirm the period reliably.

All configurations that produce smooth phase diagrams return the peaks in the $PK^{(s)}$ method. The current approach was designed to find the main variability period from the viewpoint of correlation. Indeed, the harmonic periods also provide peaks in the periodogram since the number of consecutive measurements that cross the even mean is only a small increase (see equation 7), often smaller than random crosses due to noise. Actually, other signals not related to the main variability period also can lead to smooth phase diagrams and hence they also have peaks close to $PK^{(s)}$. Moreover, incorrect periods

also can be obtained if all configurations that lead to smoother phase diagrams are not addressed.

The $PK^{(s)}$ method is a useful tool to find all periods that lead to smooth phase diagrams. Other methods, for example, the string length, or PDM method, or the fitting of truncated Fourier series also lead to smooth phase diagrams. For completeness, the most prominent peaks should be examined to evaluate the best candidate for the main variability signal. The best period can be assumed to be the one that leads to the smallest χ^2 of a model computed from the phase diagram (e.g. Drake et al. 2014; Ferreira Lopes et al. 2015a; Torrealba et al. 2015). Fig. 7 shows five cases from *CVSCI* where topics discussed here are a hindrance. In each row of panels are presented some examples as follows:

(i) *First row of panels:* stars where the $PK^{(2)}$ method does not identify the correct variability period. In these cases, an examination of the phase diagrams for the other peaks in $PK^{(2)}$ may help to find the correct value.

(ii) *Second row of panels:* stars for which a smooth phase diagram is not clearly defined by either *CVSCI* or the $PK^{(2)}$ method. Therefore, both the P_{Lit} and P_{PK} estimate may be wrong. Indeed, Drake et al. (2014) use other criteria to define the period reliably. However, this analysis is hindered if other information besides of light curve are not available.

(iii) *Third row of panels:* both the P_{Lit} and P_{PK} estimates produce smooth phase diagrams. However, they are not subharmonics of one another. This means that both periods are subharmonic of the main variability period or one of them is incorrect. Indeed, these systems also might be a complex systems with multiple periodicities, for example, an eclipsing binary where one of component is a pulsating star. These examples illustrate that the criterion of having a smooth phase diagram per se is not enough to define the variability period.

(iv) *Fourth row of panels:* the variability period found by $PK^{(2)}$ method is an overtone (greater than 2) of the variability period. Therefore, it indicates that the efficiency rate discussed in Section 4.2 is better if higher subharmonics are considered.

(v) *Last row of panels:* stars where P_{Lit} is wrong or inaccurate. P_{PK} returns smoother phase diagrams than those using P_{Lit} . Indeed, the $PK^{(s)}$ period for *CSS J110010.1 + 165359* appears to be a subharmonic of the true variability period. The wrong period determination can result in a misclassification since many of parameters used for classification are derived from the variability period.

The *WVSCI* stars have similar features to those discussed using *CVSCI* stars. A quick visual inspection was performed to support our remarks. A few stars look like those found on the last row of panels shown in Fig. 7 in both samples. Indeed, the main goal of this work is to provide a new way to find and analyse variability time-series.

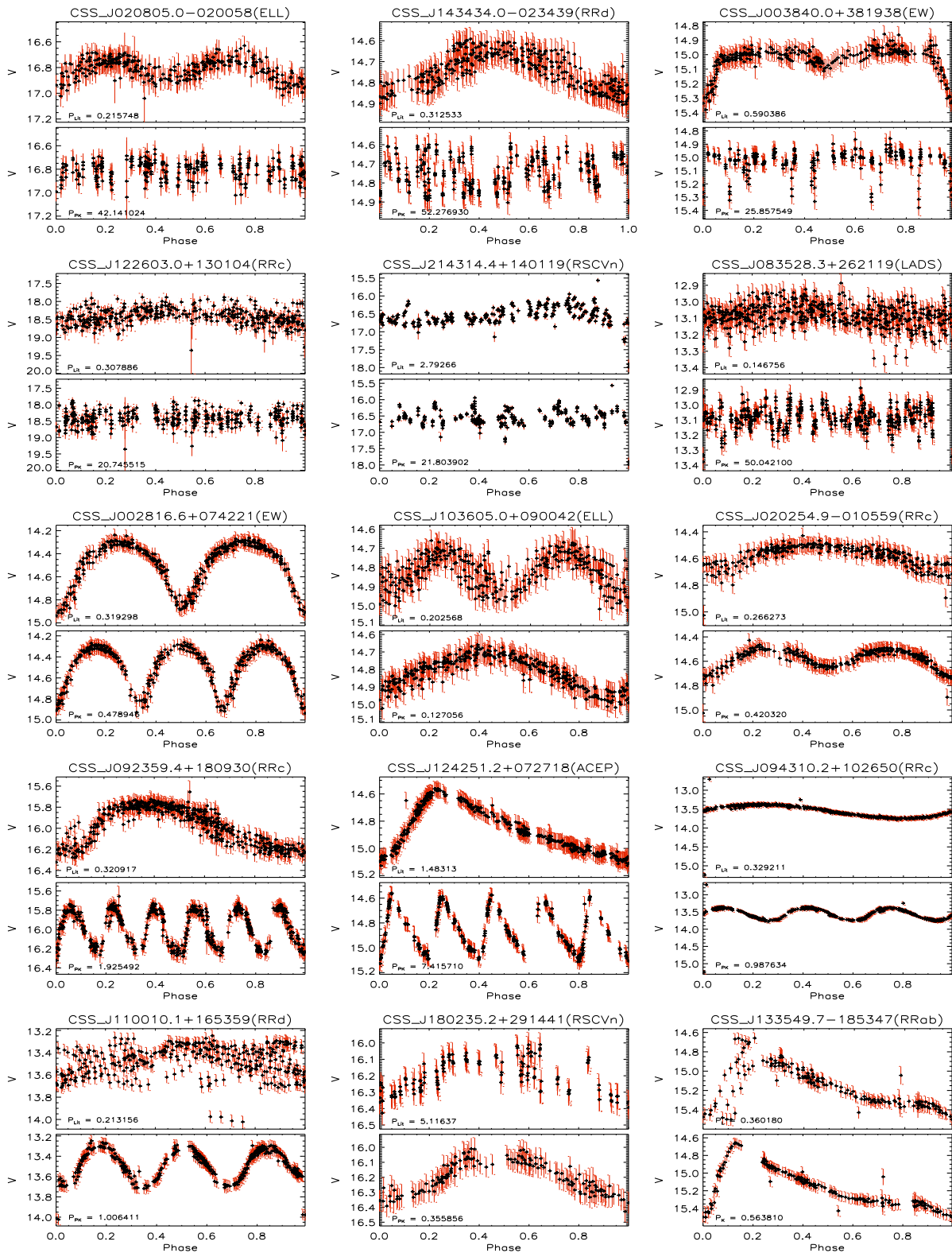


Figure 7. Phase diagrams for CVSC1 stars considering the published variability period (P_{Lit}) and that one found by $PK^{(2)}$ method (P_{PK}). The star name is shown on the top of each diagram, while the periods are in the bottom left corners.

5 CONCLUSIONS

Two new ways to search variability periods are proposed. These methods are not derived from any previous period finding method. The $PK^{(s)}$ method is characterized by presenting ordinates in the range 0–1, does not have a strong dependence on the amplitude of the signal, and also has an analytical equation to determine the FFN. Moreover, the weight of outliers is reduced since the method only considers the signs of the correlation signal. These are unique features that allow us to determine a universal false alarm probability, that is, the cut-off values that can be applied to any time-series, where it mainly depends on the S/N of the light curve. In contrast, the $PL^{(s)}$ method uses the correlation values and provides complementary information about the variability period.

The $PK^{(s)}$ and $PL^{(s)}$ methods were compared with the LSG, PDM, and SLM methods from real and simulated data having single- and multiwavelength data. As result, the efficiency rate found for LSG and PDM methods are better than all other methods for sub-samples having low (<3) or high (>3) S/N data. On the other hand, $PK^{(s)}$ and $PL^{(s)}$ efficiency is similar to that found for SLM method for data in both constraints. As expected, the accuracy of all methods is increased for data having high S/N.

In fact, the statistics considered in this paper are unlikely to be useful for data with multiple periodicities. The current methods were recent applied in the entire data of VVV survey (Ferreira Lopes et al. 2020) from where the periods estimated from five period finding method can be found. This paper is the second of this series about period search methods. Our next paper will provide our summary of recommendation to reduce running time and improve the periodicity search on big data sets.

DATA AND MATERIALS

The data underlying this article are available in the Catalina repository¹ and in the WFCAM Science Archive – WSA.² A friendly version of the data also can be shared on reasonable request to the corresponding author.

ACKNOWLEDGEMENTS

CEFL acknowledges a post-doctoral fellowship from the CNPq. NJGC acknowledges support from the UK Science and Technology Facilities Council. The authors thank to MCTIC/FINEP (CT-INFRA grant 0112052700) and the Embrace Space Weather Program for the computing facilities at INPE.

REFERENCES

- Angeloni R. et al., 2014, *A&A*, 567, A100
 Angeloni R., Di Mille F., Ferreira Lopes C. E., Masetti N., 2012, *ApJ*, 756, L21
 Bellm E. C. et al., 2019, *PASP*, 131, 018002
 Carmo A., Ferreira Lopes C. E., Papageorgiou A., Jablonski F. J., Rodrigues C. V., Drake A. J., Cross N. J. G., Catelan M., 2020, *Bol. Asoc. Argentina Astron. La Plata Argentina*, 61C, 88

- Carone L. et al., 2012, *A&A*, 538, A112
 Chadid M. et al., 2010, *A&A*, 510, A39
 Chambers K. C. et al., 2016, preprint (arXiv:1612.05560)
 Cincotta P. M., Mendez M., Nunez J. A., 1995, *ApJ*, 449, 231
 Clarke D., 2002, *A&A*, 386, 763
 Cross N. J. G., Collins R. S., Hambly N. C., Blake R. P., Read M. A., Sutorius E. T. W., Mann R. G., Williams P. M., 2009, *MNRAS*, 399, 1730
 De Medeiros J. R. et al., 2013, *A&A*, 555, A63
 Debosscher J., Sarro L. M., Aerts C., Cuypers J., Vandenbussche B., Garrido R., Solano E., 2007, *A&A*, 475, 1159
 Deeming T. J., 1975, *Ap&SS*, 36, 137
 Drake A. J. et al., 2014, *ApJS*, 213, 9
 Dupuy D. L., Hoffman G. A., 1985, *Int. Amat.-Prof. Photoelect. Photom. Commun.*, 20, 1
 Dworetzky M. M., 1983, *MNRAS*, 203, 917
 Ferreira Lopes C. E. et al., 2015b, *A&A*, 583, A122
 Ferreira Lopes C. E. et al., 2020, *MNRAS*, 496, 1730
 Ferreira Lopes C. E., Cross N. J. G., 2016, *A&A*, 586, A36
 Ferreira Lopes C. E., Cross N. J. G., 2017, *A&A*, 604, A121
 Ferreira Lopes C. E., Dékány I., Catelan M., Cross N. J. G., Angeloni R., Leão I. C., De Medeiros J. R., 2015a, *A&A*, 573, A100
 Ferreira Lopes C. E., Leão I. C., de Freitas D. B., Canto Martins B. L., Catelan M., De Medeiros J. R., 2015c, *A&A*, 583, A134
 Ferreira Lopes C. E., Cross N. J. G., Jablonski F., 2018, *MNRAS*, 481, 3083
 Hambly N. C. et al., 2008, *MNRAS*, 384, 637
 Hoaglin D. C., Mosteller F., Tukey J. W., 1983, *Understanding Robust and Exploratory Data Analysis*. John Wiley, New York
 Hodgkin S. T., Irwin M. J., Hewett P. C., Warren S. J., 2009, *MNRAS*, 394, 675
 Ivezić Z. et al., 2008, *Serb. Astron. J.*, 176, 1
 Koen C., 1990, *ApJ*, 348, 700
 Laffer J., Kinman T. D., 1965, *ApJS*, 11, 216
 Lawrence A. et al., 2007, *MNRAS*, 379, 1599
 Lomb N. R., 1976, *Ap&SS*, 39, 447
 Long J. P., Chi E. C., Baraniuk R. G., 2014, preprint (arXiv:1412.6520)
 Maciel S. C., Osorio Y. F. M., De Medeiros J. R., 2011, *New A*, 16, 68
 Minniti D. et al., 2010, *New Astron.*, 15, 433
 Mondrik N., Long J. P., Marshall J. L., 2015, *ApJ*, 811, L34
 Papageorgiou A., Catelan M., Christopoulou P.-E., Drake A. J., Djorgovski S. G., 2018, *ApJS*, 238, 4
 Paparó M. et al., 2009, *AIPC*, 1170, 240
 Paz-Chinchón F. et al., 2015, *ApJ*, 803, 69
 Gaia Collaboration et al., 2016, *A&A*, 595, A1
 Poretti E., Le Borgne J. F., Rainer M., Baglin A., Benko J. M., Debosscher J., Weiss W. W., 2015, *MNRAS*, 454, 849
 Rauer H. et al., 2014, *Exper. Astron.*, 38, 249
 Ricker G. R. et al., 2015, *J. Astron. Teles. Instrum. Syst.*, 1, 014003
 Rimoldini L., 2013, preprint (arXiv:1304.6715)
 Saha A., Vivas A. K., 2017, *AJ*, 154, 231
 Scargle J. D., 1982, *ApJ*, 263, 835
 Schwarzenberg-Czerny A., 1996, *ApJ*, 460, L107
 Stellingwerf R. F., 1978, *ApJ*, 224, 953
 Stetson P. B., 1996, *PASP*, 108, 851
 Sulis S., Mary D., Bigot L., 2017, *IEEE Trans. Signal Proces.*, 65, 2136
 Süveges M. et al., 2012, *MNRAS*, 424, 2528
 Tonry J. L. et al., 2018, *PASP*, 130, 064505
 Torrealba G. et al., 2015, *MNRAS*, 446, 2251
 VanderPlas J. T., 2018, *ApJS*, 236, 16
 VanderPlas J. T., Ivezić Ž., 2015, *ApJ*, 812, 18
 Zechmeister M., Kürster M., 2009, *A&A*, 496, 577

¹<http://nessi.cacr.caltech.edu/DataRelease/>

²<http://wsa.roe.ac.uk/>

This paper has been typeset from a $\text{\TeX}/\text{\LaTeX}$ file prepared by the author.